Available online at www.sciencedirect.com
SCIENCE DIRECT
Journal of the European Ceramic Society 26 (2006) 1159–1169
www.elsevier.com/locate/jeurceramsoc

# Stress–corrosion cracking by indentation techniques of a glass coating on Ti6Al4V for biomedical applications

J. Pavón [a,*], E. Jiménez-Piqué [a], M. Anglada [a], S. López-Esteban [b], E. Saiz [b], A.P. Tomsia [b]

[a] *Departament de Ciencia dels Materials i Enginyeria Metal.lúrgica. Universitat Politècnica de Catalunya, Avda. Diagonal 647 (ETSEIB) 08028 Barcelona, Spain*
[b] *Materials Sciences Division, Ernest Orlando Lawrence Berkeley National Laboratory, Berkeley, CA 94720, USA*

Received 4 September 2004; received in revised form 10 January 2005; accepted 23 January 2005
Available online 26 February 2005

**Abstract**

The fixation of bone replacement implants to the hosting tissue can be improved if the implants have a bioactive surface that can precipitate hydroxyapatite in vivo. Titanium alloys, despite their desirable mechanical and nontoxic properties, are not bioactive and do not bond directly to the bone. One of the ways to change a bioinert metallic surface such as a titanium alloy is to coat it with a bioactive material. This work presents the microstructural and stress–corrosion cracking characterization of two glass coatings on Ti6Al4V with different $SiO_2$ contents (61% and 64%). These coatings belong to the $SiO_2$–CaO–MgO–$Na_2O$–$K_2O$–$P_2O_5$ system and they were obtained by a simple enamelling technique. They will be used as the first layer of a bioactive multilayer system which will have an outer layer with a lower $SiO_2$ content in order to ensure the surface bioactivity. Microstructural characterization performed by scanning electron microscopy (SEM) and energy dispersive X-ray spectroscopy (EDS) shows that the coating porosity is clearly influenced by the firing time because of the longer extension of the reaction between Ti and $SiO_2$. The X-ray diffraction (XRD) integration method shows that the amount of crystalline phase (2.4CaO $0.6Na_2O$ $P_2O_5$) percentage is between 3 vol.% and 16 vol.%. After acid etching, a microstructure with clear boundaries is observed which is the result of the sintered glass particles separation. Stress–corrosion cracking was evaluated using Vickers and Hertzian (spherical) indentation, showing that both coatings are sensitive to subcritical crack growth, and that the coating with the lower silica content is more sensitive to stress–corrosion cracking. These two results are related with the larger residual stresses due to the thermal expansion mismatch. Finally, the stress–corrosion ring cracking behavior by Hertzian indentation is rationalized from the linear-elastic fracture mechanics framework.


*Keywords:* Biomedical applications; Glass; Fracture; Corrosion; Mechanical properties; Indentation

## 1. Introduction

Several important characteristics associated with Ti and Ti-based alloys—especially the balance between mechanical properties, chemical resistance, and nontoxicity—make these alloys some of the most important materials for hard tissue replacement.[1,2] However, once implanted, they become encapsulated by a dense fibrous tissue, which can result in interfacial failure and loosening of the implant.[3,4] A surface modification of the metallic implants using a bioactive material as synthetic hydroxyapatite ($Ca_{10}(PO_4)_6(OH)_2$) has been proposed to solve this problem.[3–5] Typically, hydroxyapatite (HA) is applied to Ti alloys by plasma spraying. Although several studies investigating the performance of these coatings have revealed good short-term adhesion to the bone, they also reveal poor long-term interfacial stability between the coating and the substrate.[5–7] An alternative method is to coat the metallic implants with a bioactive glass that can precipitate hydroxyapatite in vivo, optimizing at the same time the adhesion to the substrate. The first attempts to obtain a bioactive glass coating on $Ti_6Al_4V$ by enamelling, immersion in molten glass, or plasma-spray were unsuccessful because of cracking caused by stresses

* Corresponding author. Tel.: +34 934010712.
*E-mail address:* juan.jose.pavon-palacio@upc.es (J. Pavón).

0955-2219/$ – see front matter © 2005 Elsevier Ltd. All rights reserved.
doi:10.1016/j.jeurceramsoc.2005.01.045

associated with thermal expansion mismatch between the substrate and the coating.[8–10]

A simple technique for applying improved bioactive coatings on Ti-based alloys, using glasses of the $SiO_2$–CaO–MgO–$Na_2O$–$K_2O$–$P_2O_5$ system, was successfully developed at Lawrence Berkeley National Laboratory (LBNL).[11–13] The chemical composition of the glasses is based on the Bioglass® developed by Hench et al.,[11–13] with increased $SiO_2$ content, and partial substitution of the original $K_2O$ and MgO with $Na_2O$ and CaO, respectively. These changes were done in order to reduce the coating thermal expansion coefficient so that it would be closer to that of the substrate.

Concentrated and constantly applied loads during extended periods of time are one of the most severe mechanical requirements for a coated metallic implant.[15] If the environment in which this kind of load acts is chemically aggressive, the load effect can be enhanced, creating and propagating cracks. Therefore, it is important to know how this kind of biomaterials behave under these specific mechanical conditions. Indeed, the fundamental aim of the work reported herein is to evaluate the stress–corrosion cracking behavior of two glass coatings on Ti6Al4V using Vickers and Hertzian (spherical) indentation techniques. These coatings have different $SiO_2$ contents (61% for 6P61 and 64% for 6P64). Both of them are candidates to form the primary layer in direct contact with the substrate, while an outer layer, with a lower $SiO_2$ content, will ensure the surface bioactivity.[8] This system will improve the interfacial mechanical stability between the coating and the substrate and will also optimize the fixation between the implant and the bone.

## 2. Experimental procedure

### 2.1. Sample preparation

The coatings were obtained using a conventional enamelling method.[11–13] The starting glasses were obtained by mixing the appropriate reagents ($SiO_2$: 99.5%, Cerac; $CaCO_3$: 99.9%, JT Baker; MgO: 98.6%, JT Baker; $K_2CO_3$: 99.0%, Allied Chemical; $NaHCO_3$: 99.5%; JT Baker; and $NaPO_3$: 99.7% Allied Chemical) in ethanol using a high-speed stirrer to achieve the desired composition for each glass (Table 1). The mixture was first dried at 80 °C for 12 h and then air-fired at temperatures ranging from 1400 °C to 1500 °C for 4 h in a Pt crucible. The melt was cast into a graphite mold to obtain glass plates (~50 mm × 50 mm × 5 mm) that were subsequently annealed at 500 °C for 6 h to relieve stresses and then milled in a planetary agate mill. To obtain the coatings, a suspension of the glass powder (particle size < 20 μm) in ethanol was deposited on Ti6Al4V beams (99.0% purity, 45 mm × 5 mm × 4 mm), which had been previously polished with diamond (1 μm particle size) and cleaned in ultrasonic baths of acetone and ethanol. Afterwards, the coatings were air-dried at 75 °C overnight and fired at temperatures ranging from 800 °C to 820 °C for a short time (around 1 s). Finally, the coatings were quenched in air. The initial beams were sectioned into samples of 5 mm × 3 mm × 4 mm to allow observation of the coatings' cross-section and the making of indentation tests.

Table 1
Chemical composition of the glass coatings

| Composition (wt.%) | $SiO_2$ | CaO | $Na_2O$ | MgO | $P_2O_5$ | $K_2O$ |
|---|---|---|---|---|---|---|
| 6P61 | 61.1 | 12.6 | 10.3 | 7.2 | 6.0 | 2.8 |
| 6P64 | 64.1 | 11.6 | 9.8 | 6.3 | 6.0 | 2.7 |

### 2.2. Microstructural characterization

Coating thickness was measured using optical microscopy by observations of the coatings' cross-section using image analyser software. This method was also used to observe the coating microstructure revealed after acid etching (10 ml $HNO_3$, 6 ml HF and 80 ml $H_2O$). SEM and EDS analysis was also performed on the samples surface and cross-sections. The X-ray diffraction patterns of the coatings were obtained using a powder diffractometer of Bragg-Brentano $\theta/2\theta$ geometry (Siemens D-500) coupled with a graphite secondary monochromator. The radiation used was Cu Kα ($\lambda = 1.5418$ Å). The amount of crystalline phase was calculated by the peaks integration method.[16] Coating porosity was estimated by surface image analysis.

### 2.3. Mechanical testing

The coatings' roughness parameters ($R_a$ = profile deviations mean and $S$ = mean space between the profile peaks) were measured with a Surftest SV-502 bidimensional surface tester with a diamond stylus. The coatings' subcritical crack growth in ambient air (relative humidity ~40%) was evaluated from Vickers indentation cracks with applied loads of 1.96, 2.94 and 4.90 N, measuring the change in lengths of the cracks that emanate from the imprint corners at increasing time intervals up to 78 h. The residual stresses due the thermal expansion mismatch between the coating and the substrate were estimated using the X-ray diffraction method ($\sin^2\psi$) which consists in measuring the interplanar distance variation of a set of parallel planes, $h\,k\,l$, for different incident angles.[17–19] This technique allows to calculate the elastic deformation of the crystalline network at the thin surface layer. These measured residual stresses are analysed in terms of the subcritical crack growth, the difference in thermal expansion coefficients and the micro cracking observed in the coatings by SEM backscattered electrons technique. The Hertzian (spherical) indentation tests were carried out with WC-Co spheres using an universal electromechanical Instron machine (model 8562) with a 1 kN load cell (Fig. 1). The radius of the spheres was 1.25 mm and the monotonic applied load rate used to measure the critical loads for cone

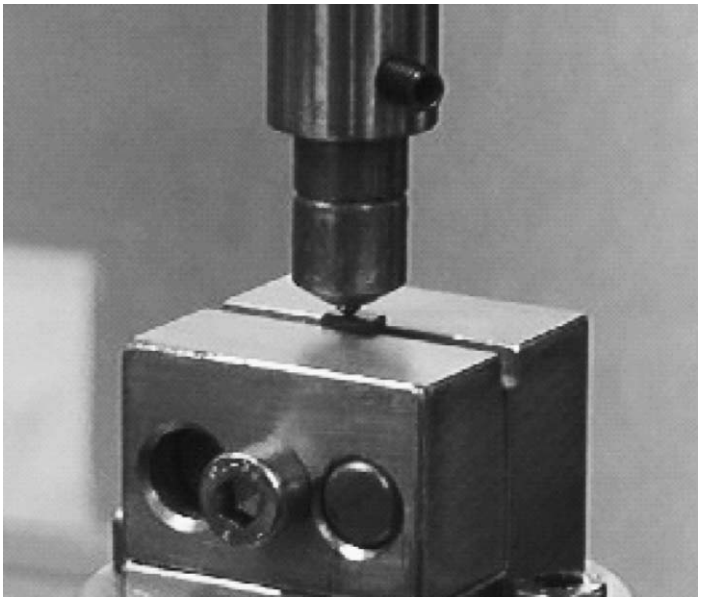

Fig. 1. Mechanical set-up for the Hertzian indentation test.

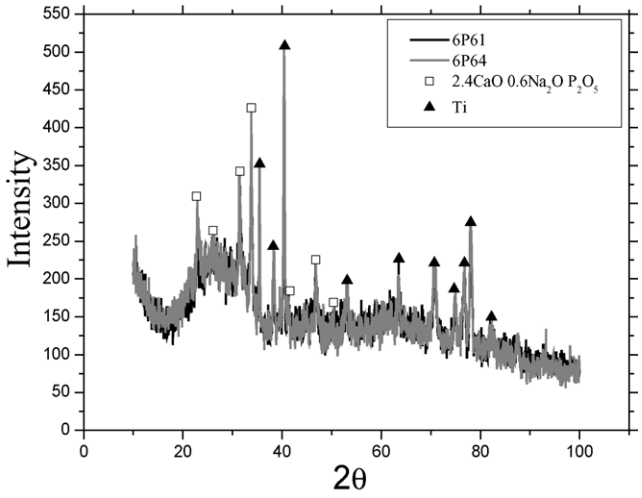


Fig. 3. X-ray diffraction patterns of 6P61 and 6P64 coatings showing the presence of crystalline phase.

and radial crack formation, $P_{cc}$ and $P_{rc}$, respectively, was $2\,N\,s^{-1}$. To study the stress–corrosion cracking, the constant applied loads were fractions of $P_{cc}$ (60% to 90%), determining a critical contact time, $t_f$, for ring crack formation. This event was observed by optical microscopy and image analysis immediately after the load was removed.

## 3. Results and discussion

### 3.1. Microstructural characterization

The thickness measurements were carried out in 10 different positions using 12 samples of each coating, and they were very similar for both coatings (6P61 = 40 ± 3 μm; 6P64 = 41 ± 5 μm). Fig. 2a shows the main parameters of the porosity estimation by optical microscopy. Despite this measurement can be influenced by the different diffraction indexes between the glass and the air bubbles, the measurement of some pore size by SEM (Fig. 7) gives values similar to those estimated by optical microscopy, and therefore the measurement can be considered valid. Fig. 2a also includes the 6P61 coating with a 15 s firing time, which exhibits larger porosity than the two coatings with minimum firing time. This higher porosity is due the longer time for reaction between the Ti and $SiO_2$ in the glass, which typically produce relatively large bubbles (Fig. 3):[11]

$$5Ti + 3SiO_{2(glass)} = Ti_5Si_3 + 3O_{2(gas)} \quad (1)$$

The other important source of porosity is the air bubbles trapped between the glass particles (small pores in Fig. 2b), which can be reduced by increasing the firing time because of the more extensive glass sintering and gas evolution to the outside of the sintered body. However, according to Fig. 2a, bubbles which are originated from the reaction of Eq. (1) have the predominant role. Note that the SEM photograph of the

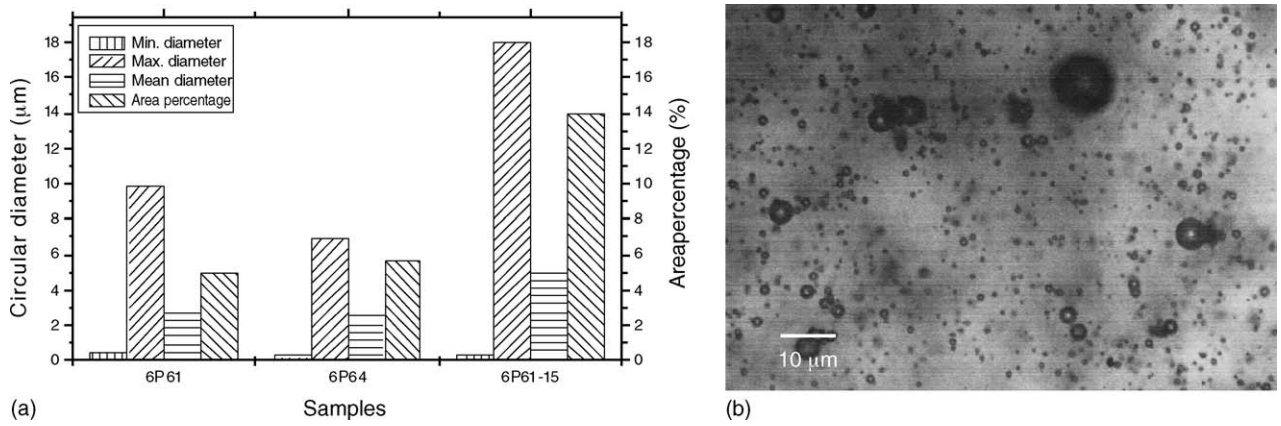


Fig. 2. Coatings porosity measured by image analysis: (a) porosity percentage and pore size of 6P61 and 6P64 coatings (around 1 s firing time) and 6P61 with 15 s firing time; (b) top view of 6P61 coating with 15 s firing time where the porosity can be easily appreciated.

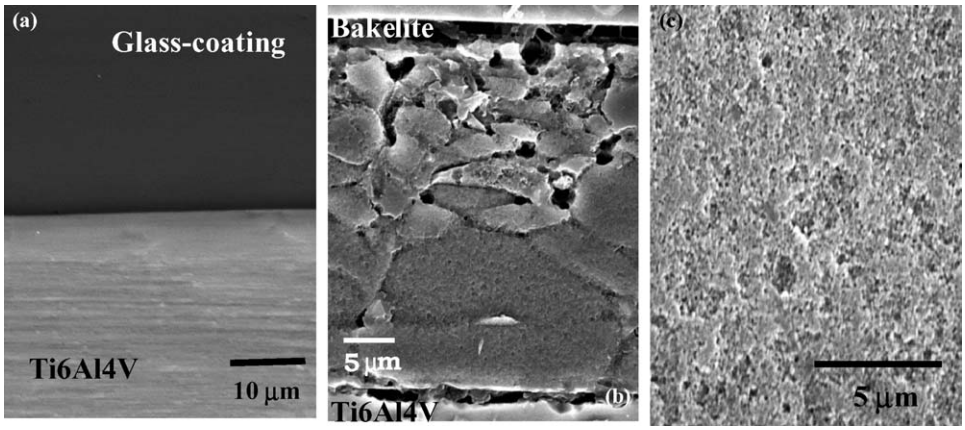


Fig. 4. SEM micrographs of the 6P61: (a) coating cross-section polished; (b) coating cross-section polished and etched; (c) fused glass.

6P61 coating cross-section (minimum firing time; Fig. 4a) does not show any pore. Therefore, the observed porosity by optical microscopy is confined at the coating surface. This confirms that the porosity for minimum firing time is mainly due to air bubbles trapped during sintering.

Previous studies have reported sodium calcium phosphate, 2.4CaO 0.6$Na_2O$ $P_2O_5$, as the main crystalline phase in the coatings.[11–13] The X-ray diffraction patterns obtained in this work show the same phase in both coatings (Fig. 3). The Ti peaks observed in the patterns are diffracted from the substrate due the low X-ray absorption of the glass coatings.

The amount of crystalline phase was estimated by the diffraction peaks integration method[16] and the results are summarized in Table 2. These values include the porosity correction, and they are presented as ranges using the double peak integration method, which considers the influence of both coating and substrate background. This allows the establishment of a limit for the amount of crystalline phase. The upper limit difference observed in Table 2 is caused by the small thickness difference between the tested samples, which clearly influences the background response of the coatings. Therefore, the volume percent of the crystalline phase for both coatings is practically the same.

The acid etching of the coatings' cross-section revealed the same microstructure for both (Fig. 4b), which is the result of preferential etching at the boundaries between sintered glass particles due to the higher dissolution rates in these areas.[8] Consequently, etching of the 6P61 fused glass did not reveal any microstructure (Fig. 4c). Larger particles are in contact with the substrate as a result of the faster sedimentation rates during coating (Fig. 4b).

Table 2
Crystalline phase percentage estimated by the peak integration method

| | 6P61 | 6P64 |
|---|---|---|
| Crystalline phase percentage, 2.4CaO 0.6$Na_2O$ $P_2O_5$ (vol.%) | 3.2–11.3 | 3.1–16.1 |

### 3.2. Mechanical testing

After evaluation of the roughness parameters ($R_{a6P61}$ = 0.51 μm; $R_{a6P64}$ = 0.21 μm; $S_{6P61}$ = 86.83 μm; $S_{6P64}$ = 110.60 μm), it was concluded that indenting the samples without polishing, would yield similar results that indenting a polished surface;[20] consequently all samples were tested unpolished. Fig. 5 presents the results of Vickers indentation subcritical crack growth in ambient air (relative humidity ≈40%). For both the 6P61 and 6P64 coatings, it can be observed that the crack velocity is considerably higher for a short time after indenting, then decreases almost to zero, following the basic power law function:

$$\upsilon = \upsilon_0 \left( \frac{K_a}{K_{Ic}} \right)^n, K_a < K_{Ic} \quad (2)$$

where $\upsilon$ is the crack velocity, $\upsilon_0$ is the velocity coefficient, $K_a$ is the applied stress intensity factor, $K_{Ic}$ is the coating fracture toughness and $n$ is the velocity exponent. Fig. 5 also clearly shows that cracks in the 6P61 coating are longer than

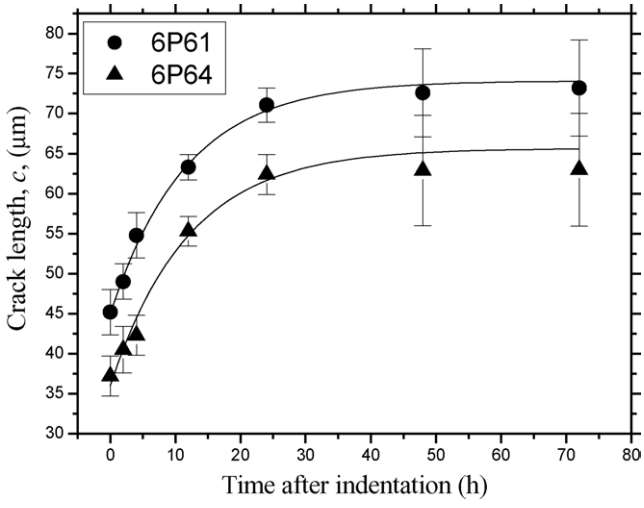


Fig. 5. Vickers indentation subcritical crack growth for an applied load of 1.96 N.

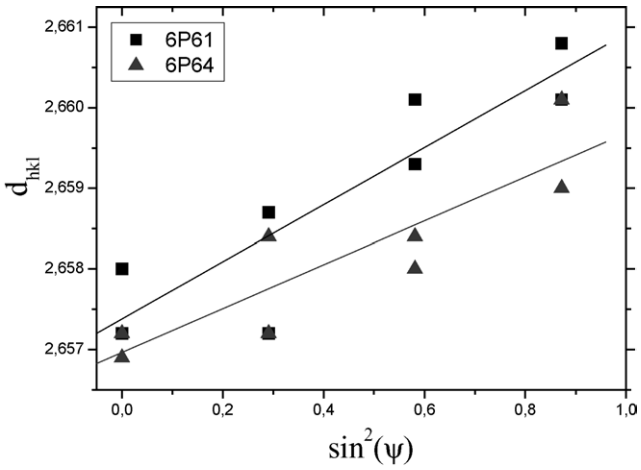


Fig. 6. Interplanar distances for different incident angles in function of the $\sin^2\psi$.

in 6P64 after indentation. This difference is due to the larger tensile residual stresses of 6P61, which is discussed below.

### 3.2.1. Residual stress measurements

The X-ray diffraction $\sin^2\psi$ method was used to estimate the residual stresses of the crystalline phase. Fig. 6 shows the interplanar distances, $d_{hkl}$, in terms of $\sin^2\psi$, where $\psi$ is the variable angle between the normal to the diffracting lattice planes and the sample surface. In this figure, the slope of both curves is positive, which means that the crystalline phase ($2.4CaO\ 0.6Na_2O\ P_2O_5$) is subjected to tensile residual stresses in both coatings. For the crystalline phase of 6P61 coating, the larger slope could be related with the longer crack length difference from the subcritical crack growth results (Fig. 5). However, this slope trend is not enough to determine the average residual stress of the coatings because of the influence of the thermal expansion mismatch between the crystalline and the amorphous phase. Therefore, a better approach can be made by calculating the difference in the residual stress of the coatings from the following expression for the theoretical residual-macro-stress due to the thermal expansion mismatch:[21]

$$\sigma_{res} = \frac{\Delta T(\alpha_c - \alpha_s)E_c}{(1-\nu_c)(1+(1-\nu_s(E_c d_c)/1-\nu_c(E_s d_s)))} \quad (3)$$

where $\Delta T$ is the difference in temperatures between the glass softening temperature and room temperature, $\alpha$ is the thermal expansion coefficient ($c$ and $s$ sub-index denotes coating and substrate respectively), $\nu$ is the Poisson's ratio, $E$ is the Young modulus and $d$ is the thickness. Considering that $E_s d_s \gg E_c d_c$ and that the elastic constants of the coatings are practically the same due to similar compositions,[8] it can be shown that the difference in residual stress between the coatings is:

$$\sigma_{res}]_{6P61} - \sigma_{res}]_{6P64} = \frac{\Delta T E(\alpha_{6P61} - \alpha_{6P64})}{1-\nu} \quad (4)$$

Table 3 presents different results from Eq. (4), by taking $T = 623\,^\circ C$[22] as softening temperature (room temperature equal to 25 °C), $E = 70{,}000$ MPa measured by nanoindentation technique, $\nu = 0.25$[8] and pairs of thermal expansion coefficients experimentally determined[22] and predicted using different models[23–26] as was previously considered in.[22] These results confirm that there is a clear and non-negligible difference in the residual stress of the coatings. Finally, by looking at Fig. 7, which shows microcracking of both coatings detected by the backscattered electron images, it is clear that cracks in the 6P61 coating are longer than those in the 6P64 coating. This finding confirms that the

Table 3
Difference in thermal residual stresses between the coatings estimated from Eq. (4) for $\alpha$ values experimentally measured and predicted using different models

| | $\alpha_{6P61}$ ($10^{-6}\,^\circ C^{-1}$) | $\alpha_{6P64}$ ($10^{-6}\,^\circ C^{-1}$) | $\sigma_{res}]_{6P61} - \sigma_{res}]_{6P64}$ (MPa) |
|---|---|---|---|
| Guard and Dubrull[23] | 10.5 | 9.8 | 39.7 |
| Hall[24] | 9.8 | 9.4 | 22.7 |
| English and Turner[25] | 9.5 | 9.0 | 28.4 |
| Winkelmann and Schott[26] | 10.1 | 9.7 | 22.7 |
| Experimental[22] | 10.2 | 9.1 | 61.4 |

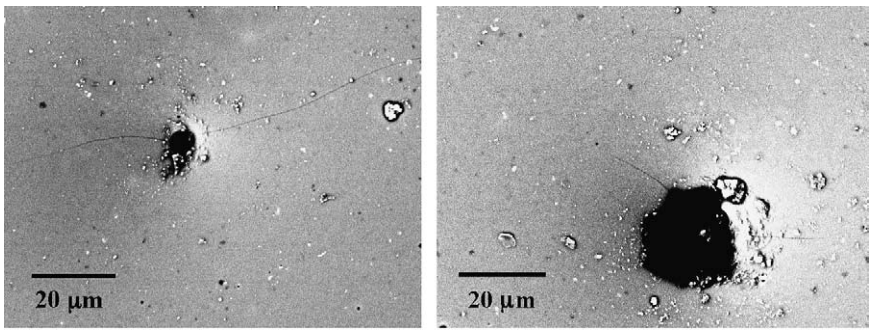


Fig. 7. SEM backscattered electrons photograph showing the coatings cracks emanating from the pores: (a) 6P61 coating; (b) 6P64 coating.

Table 4
Critical loads for cone and radial cracks by a monotonic Hertzian indentation

| | 6P61 | 6P64 |
|---|---|---|
| Cone crack critical load, $P_{cc}^{A}$, (N) | $42 \pm 1$ | $50 \pm 2$ |
| Radial crack critical load, $P_{rc}$ (N) | $62 \pm 2$ | $60 \pm 2$ |

coatings are under different residual stresses where the 6P61 coating presents the higher stress, which is consistent with its larger thermal expansion mismatch with Ti6Al4V substrate ($10.2 \times 10^{-6}\,^{\circ}C^{-1}$ against $(9.1–9.8) \times 10^{-6}\,^{\circ}C^{-1}$).

### 3.2.2. Stress–corrosion cracking tests

It is well known that damage during an Hertzian monotonic indentation test on a brittle coating/ductile substrate system ($E_c < E_s$) occurs by a series of steps:[27,28]

1. Ring cracking at a load for which a pre-existent surface flaw "runs around" to form a shallow ring. The surface flaw is located close to the contact perimeter over which the contact tensile stress is at maximum.
2. Cone cracking happens when the increasing load reaches a second critical value and the "ring" begins to flare out into the frustum of a cone.
3. Radial cracking then appears from the interfacial flaws on the central contact axis due to the maximum biaxial bending stress that acts over this axis.
4. Plastic deformation of the substrate occurs for sufficiently higher applied loads.

The first step of these tests was to determine the apparent critical loads for cone cracking, $P_{cc}^{A}$; and the results are shown in Table 4. Both cone and radial crack morphologies, used as criteria to obtain the values in this table, are illustrated in Fig. 8. The critical load for radial cracking, $P_{rc}$, of both coatings is very similar. This is not surprising because $P_{rc}$ depends on the square of the coating thickness,[27] which is practically the same for both coatings (see 3.1). Note that the single value of cone cracking critical load ($P_{cc}^{0}$) is directly related with the square of the fracture toughness.[29] Then, the difference in critical loads given in Table 4 can only be explained by the existence of different values for the residual stresses in each coating. It is believed that the small different chemical composition of the coatings does not have so such large influence in their fracture toughness. This can be confirmed with the method proposed by Roberts et al.[30] to determine the surface residual stresses in brittle materials by Hertzian indentation. The stress intensity equilibrium condition (when a pre-existing surface flaw at the contact circle grows in an unstable manner and forms a ring crack during a monotonic test) is given by:

$$K_{Ia} = K_{Ic}^{A} + K_{\sigma_{res}} = K_{Ic}^{0} \tag{5}$$

where $K_{Ia}$ is the total applied stress intensity factor, $K_{Ic}^{A}$ is the apparent value of fracture toughness, $K_{\sigma res}$ is the stress intensity factor due to the surface residual stress which is assumed to be biaxial and uniform trough the depth, and $K_{Ic}^{0}$ is the fracture toughness of the stress-free material. Because of the small chemical composition difference between the coatings, it is assumed that $K_{Ic}^{0}]_{6P61} \cong K_{Ic}^{0}]_{6P64}$. Then, from Eq. (5):

$$K_{Ic}^{A}]_{6P64} - K_{Ic}^{A}]_{6P61} = K_{\sigma res}]_{6P61} - K_{\sigma res}]_{6P64} \tag{6}$$

The apparent fracture toughness by Hertzian indentation, $K_{Ic}^{A}$, can be expressed according to Warren[29] as:

$$K_{Ic}^{A} = \left(\frac{E^{*} P_{cc}^{A}}{Cr}\right)^{1/2} \tag{7}$$

where $P_{cc}^{A}$ is the apparent critical load for cone crack formation, $E^{*}$ is the "effective Young's modulus" ($E^{*} = (1 - \nu_i^2/E_i + 1 - \nu_c^2/E_c)^{-1}$ and $r$ is the radius of the sphere. In addition, $C$ is a dimensionless constant that depends on the critical flaw size–contact radius ratio ($c^{*}/r_c$), the critical flaw position-contact radius ratio ($r^{*}/r_c$), indenter and material Poisson's ratios ($\nu_i$ and $\nu_s$), and the elastic mismatch between the sphere and the tested material (characterized by the Dundurs constant $\beta$ and the coefficient of friction, $f$). This constant, $C$, takes into account the influence in the stress intensity factor of the steep gradient of stress in radial direction for a small surface flaw. Warren determined this constant using the distributed dislocation method[29] and he showed that at a given Hertzian crack critical load, $P_c$, there is a flaw with a combination of size and position that gives a maximum value

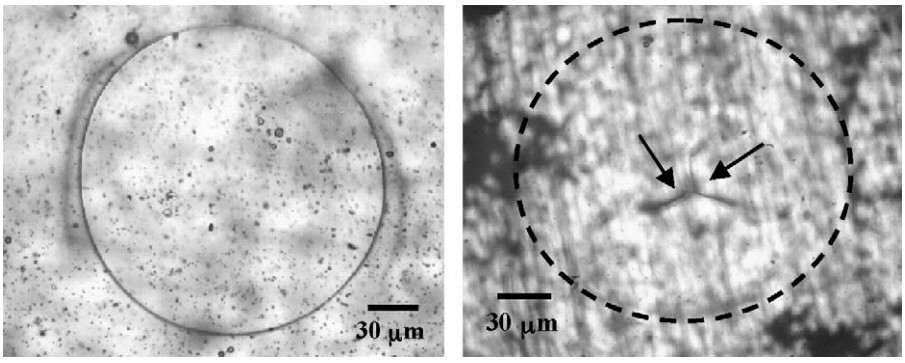


Fig. 8. Cone and radial cracks morphologies of the 6P61 coating after a monotonic Hertzian indentation test.

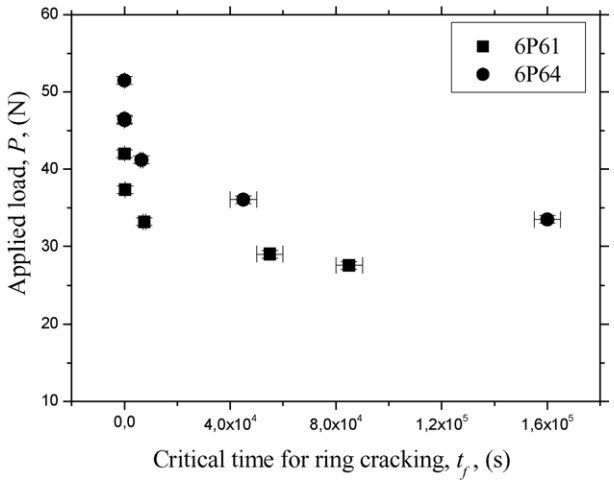


Fig. 9. Experimental results of stress–corrosion ring cracking.

of $K_{Ia}$, since $c^*/r_c$ and $r^*/r_c$ depend only on $\nu_i$ and $\nu_s$. For the system WC-Co indenter/glass coating, $C = 4179$.[30]

The stress intensity factor induced on the pre-existent surface crack by the residual stress is:

$$K_{\sigma_{res}} = 1.29\sigma_{res}(a)^{1/2} \quad (8)$$

where $a$ is the depth of the crack and $\sigma_{res}$ is the surface stress assumed to be biaxial and uniform over the crack depth. After replacement of (7) and (8) in Equation (6), the difference between the residual stress of the coatings can be expressed as:

$$\sigma_{res}]_{6P61} - \sigma_{res}]_{6P64} = \frac{1}{0.7}\left(\frac{E^*}{C\pi ar}\right)^{1/2}[(P^A_{cc6P64})^{1/2} - (P^A_{cc6P61})^{1/2}] \quad (9)$$

where $E^*$ is the "effective Young's modulus" (66784 MPa), $C$ depends on the relative elastic properties of indenter and coating ($C = 4179$), $a$ is the mean size of the surface flaw (~2 μm, Fig. 2), $r$ is the radius of the sphere ($r = 1.25$ mm) and $P^A_{cc6P61}$ and $P^A_{cc6P64}$ are the apparent cone cracking critical loads for the 6P61 and 6P64 coatings, respectively (Table 4). From this relationship, the difference in residual stresses between the coatings can be evaluated to be, approximately, 37 MPa. This result is in good agreement with the difference in residual stresses calculated from the Eq. (4) (Table 3).

Fig. 9 presents the stress–corrosion cracking results showing the constant applied load (lower than $P^A_{cc}$) as a function of the critical contact time to produce the ring cracking. It is clear that both coatings are sensitive to stress–corrosion cracking and also that the 6P64 shows higher resistance to ring cracking. This result is consistent with the higher $P^A_{cc}$ value and also with the lower residual stresses calculated in 6P64.

The following analysis of the spherical contact degradation is based on the indentation fracture mechanics framework, specifically on the previous work of Licht et al.[31] It

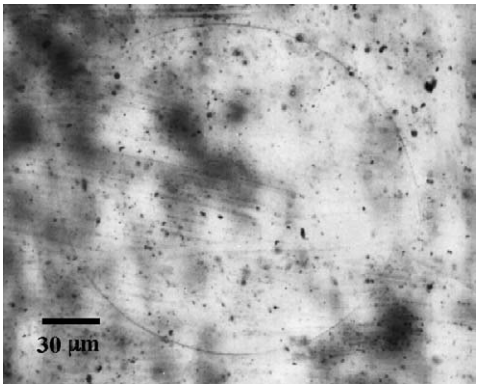


Fig. 10. Ring crack morphology used as degradation criteria during the Hertzian indentation stress–corrosion tests.

is assumed that the coatings are brittle and their degradation is exclusively produced from ring cracking, as can be seen in Fig. 10. It is also assumed that a pre-existing surface flaw suffers subcritical crack growth during the static contact according to the basic power-law crack velocity function (Eq. (2)). Furthermore, the analysis is focused on the cone cracking initiation stage, i.e., ring crack formation, which is the typical damage stage observed after removing the contact load (Fig. 10).

Recalling Eq. (5), the total stress intensity factor applied on a semicircular surface crack at the contact circle is given by:

$$K_I^{A,B} = K_{I,H}^{A,B} + K_{I,\sigma_{res}}^{A,B} \quad (10)$$

where $K_{I,H}$ and $K_{I,\sigma_{res}}$ are the stress intensity factors due to Hertzian contact loads and to the residual stresses, respectively. $A$ and $B$ denote the deepest and surface points of the crack (Fig. 11). The radial stress component of the contact stress field at the initial surface crack position ($x = r_0$) along the $z$ direction (depth) changes rapidly from a maximum tensile stress at the surface to a compressive stress deeper inside the material (Fig. 12). This stress distribution can be fitted by a polynomial:[31]

$$\sigma_{(z)} = \sum_{i=0}^{n} \sigma_i \left(\frac{z}{a}\right)^i \quad (11)$$

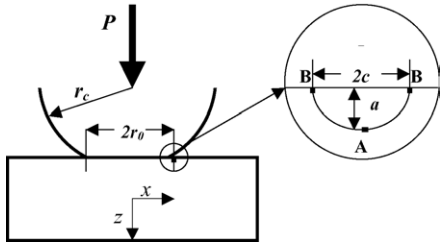


Fig. 11. Schematic of Hertzian contact test and a semi-elliptical surface crack close to the contact circle and initiation site of a ring crack.

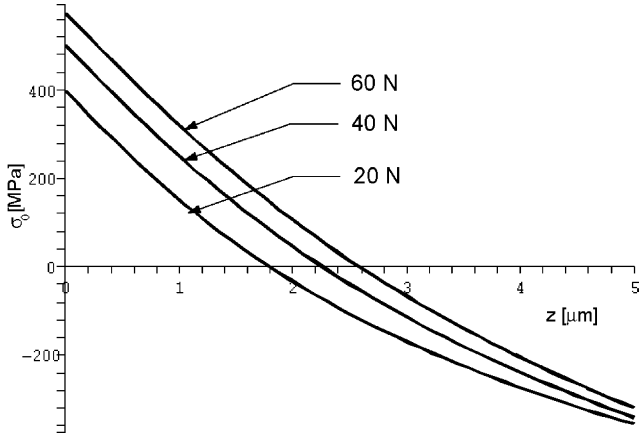


Fig. 12. Stress field distribution along $z$ direction at $x = r_c$ of the radial tensile component from the contact Hertzian on the coating for $P = 20$ N, 40 N and 60 N estimated from the Huber solutions of the Hertzian elastic stress field[32].

Then, the stress intensity factor in Eq. (10) can be expressed as:

$$K_{I,H}^{A,B} = (\pi a)^{1/2} \sum_{i=0}^{n} \sigma_i \left(\frac{z}{a}\right)^i f_i^{A,B}\left(\frac{a}{t}, \frac{c}{a}\right) \tag{12}$$

where $f_i^{A,B}$ is the geometrical function of the stress intensity factor which depends on eccentricity, ($c/a$); and $t$ is the specimen thickness (for a semi-infinite solid, $a/t \cong 0$). Assuming that the radial stress distribution shown in Fig. 12 is approximately linear within small distances (crack depth $\ll$ contact radius, $a \ll r_c$) and vanishes at $z = a$, the following is obtained:

$$\sigma_{(z)} = \sigma_0 - \sigma_0 \left(\frac{z}{a}\right) \tag{13}$$

where $\sigma_0$ is the maximum radial tensile stress acting at the surface coordinate $r_0$, where the surface crack is located. This stress can be expressed as a function of the $r_0$, the applied load, $P$, and the Poisson's ratio of the material, $\nu$:[34]

$$\sigma_0 = \frac{(1-2\nu)P}{2\pi r_0^2} \tag{14}$$

Therefore, stress intensity factor in Eq. (12) can be reduced to:

$$K_{I,H}^{A,B} = (\pi a)^{1/2} \sigma_0 \left[f_0^{A,B}\left(\frac{c}{a}\right) - f_1^{A,B}\left(\frac{c}{a}\right)\right] \tag{15}$$

where $f_0$ and $f_1$ are the geometrical functions of the stress intensity factor for $z = 0$ and $z = a$, respectively.

For a porous material, like the one described here, when the ring crack is completed after the environmental assisted crack growth, it is assumed that there is not crack growth in $z$ direction (depth) because the critical condition to start growth in this direction is not reached. For example, for a typical initial crack depth ($a_0$) as large as 2 μm (see Fig. 13), the critical ratio to start growth in $z$ direction ($(c/a)_c$), where $K_A = K_B$,[31] would be less than 0.001; then $c_f$ would be larger than 1000 μm. This value is far larger than $c_f$, which was observed experimentally from the ring crack radius (between

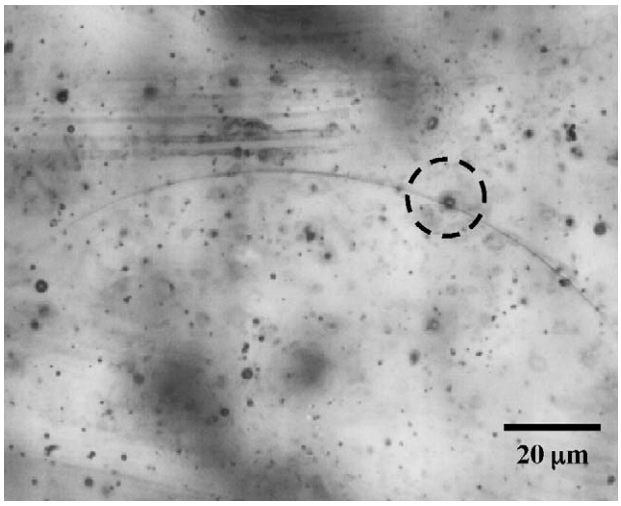


Fig. 13. Surface flaw (pore) from which the ring crack is formed under static contact load.

200 and 250 μm). Therefore, since $a$ is constant, the analysis is focused on the $K_I^B$. Indeed, the stress intensity factor due to the residual stresses is given by:

$$K_{\sigma_{res}} = (\pi a)^{1/2} \sigma_{res} f_0^B \left(\frac{c}{a}\right) \tag{16}$$

and, by combining Eqs. (15) and (16), the applied stress intensity factor in $B$ can be obtained as:

$$K_I^B = (\pi a)^{1/2} f_0^B \left[\sigma_{res} + \sigma_0 \left(\frac{f_0^B - f_1^B}{f_0^B}\right)\right] \tag{17}$$

and from $f_0^B$ and $f_1^B$ (Fig. 14) it can be seen that $(f_0^B - f_1^B/f_0^B)$ is a weak function of eccentricity that can be replaced by a constant equal to 5/6, and Eq. (17) is thus reduced to:

$$K_I^B = (\pi a)^{1/2} f_0^B [0.8\sigma_0 + \sigma_{res}] \tag{18}$$

From Fig. 14, $f_0^B$ can be approximated by a straight line, $f_0^B \approx 0.8 - 0.03(c/a)$, for a $c/a$ range given by the experi-

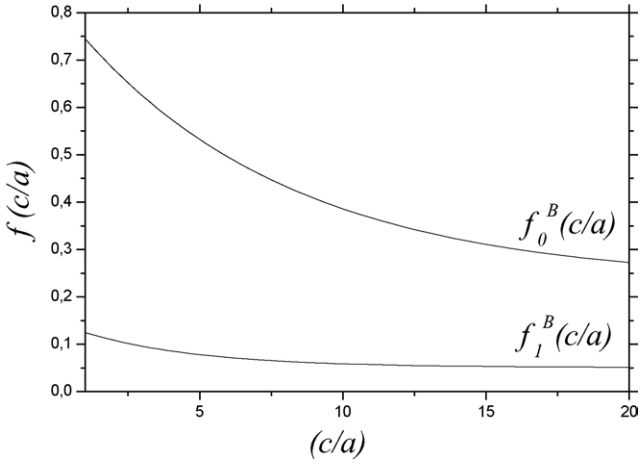


Fig. 14. Ellipticity functions of the stress intensity factor for the maximum and minimum values of the radial tensile stress due to the Hertzian contacts.[33]

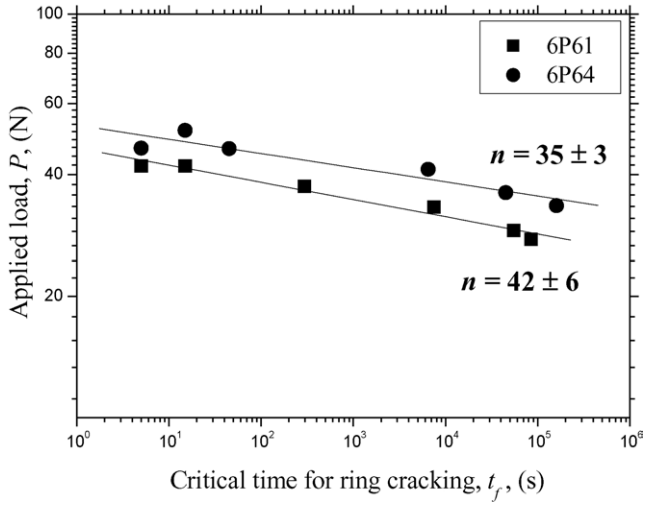


Fig. 15. Plot of $\log P - \log t_f$ from the experimental stress–corrosion cracking results (Fig. 9 and estimation of the crack velocity exponent, $n$, according to Eq. (22).

mental results. By replacing Eq. (18) in the crack velocity function—Eq. (2)—the following is obtained:

$$\frac{dc}{dt} = \upsilon_0 \left[ \frac{(\pi a)^{1/2} f_0^B (0.8\sigma_0 + \sigma_{res})}{K_{Ic}^0} \right]^n \quad (19)$$

This equation is solved assuming that the ring crack is formed by the extension of an initial semicircular surface crack with a surface length equal to $a$. Since the location of the initial crack, $r_0$, is about 12% larger than the contact radius,[29,35] $c_f \cong 1{,}12\lambda\pi r_c$, where $r_c$ is the contact radius given by:

$$r_c = \left( \frac{3rP}{4E^*} \right)^{1/3} \quad (20)$$

The constant $\lambda$ is the fraction of the half ring crack length when the growing crack from the initial flaw, coalesces with other crack or reach the stress–corrosion threshold, $K_{th}$. Considering that in ceramics normally $K_{th} \approx 0.5K_{Ic}$, this explains why $0 < \lambda < 1$, because for $\lambda = 1$, $K_I^B \ll 0.5K_{Ic}$ (from Eq. (18)). This analysis is consistent with the previous assumption of not crack growth in $z$ direction.

Therefore, by solving Eq. (19) using Eq. (20), it can be shown that:

$$P^{2n/3} A^n \left( 1 + \frac{\sigma_{res}}{0.8\sigma_0} \right)^n t_f = \alpha \quad (21)$$

where $A = 0.8(1–2\nu)(4E^*)^{2/3}/2\pi(3r)^{2/3}$ and $\alpha$ is a constant which depends only on the material and indenter properties, $\alpha = f(a, E^*, \upsilon_0, K_{Ic}^0, r)$. Then, for $\sigma_{res} = 0$, Eq. (21) is reduced to:

$$P^{\frac{2n}{3}} t_f = \frac{\alpha}{A^n} \quad (22)$$

Fig. 15 shows the plotting of $\log P$ versus $\log t_f$ from the experimental results of Fig. 9 and the experimental slopes gives acceptable values of the crack velocity exponent, $n$, according to Eq. (22). These $n$ values are in good agreement with previous results of Barry et al.[36] using DCB samples of a Bioglass® in air ($n \approx 30$). On the other hand, for the case of $\sigma_{res} \neq 0$, Eq. (21) can be expressed as:

$$\sigma_{eff}^n t_f = \alpha \quad (23)$$

where $\sigma_{eff} = P^{1/3}\sigma_{res} + AP^{2/3}$. The $n$ values obtained by plotting $\log \sigma_{eff}$ versus $\log t_f$, using an estimation of residual stresses due to the thermal expansion mismatch—Eq. (3)—($\sigma_{res6P61} = (+)$ 40.3 MPa and $\sigma_{res6P64} = (-)$ 10.8 MPa), are reasonably good ($n_{6P61} = 46 \pm 7$ and $n_{6P64} = 40 \pm 3$). Finally, note that all $n$ estimations are higher than 30 which is the result obtained by Barry et al.[36] for Bioglass® in air. This difference is due to the higher $SiO_2$ content of the coatings (61% and 64%), compared with 45% for Bioglass®, and it is recognized that the corrosion resistance of this type of glass is strongly dependent on the $SiO_2$ content.[3,8,14]

Since there is an acceptable consistency between the crack velocity exponent estimation from the Eqs. (22) and (23), the stress–corrosion ring cracking of a porous glass coating can be rationalized from the Hertzian indentation fracture mechanics, where the ring crack is formed from a pore sufficiently large to not grow in $z$ direction inside the material. This analysis also confirms the clear influence of residual stresses of the coatings in their stress–corrosion behaviour, especially for lower contact loads, when the residual stresses have a dominant role.

## 4. Conclusions

In this work, the microstructural characterization and the stress–corrosion cracking evaluation of two glass-based coatings on Ti6Al4V with different $SiO_2$ content (61% and 64%) were carried out. These coatings were designed to be the primary layer, in direct contact with the metallic substrate, of a multilayer functionally graded material (FGM), which will have a bioactivity surface to improve the implant fixation to the bone.

These coatings are composed of glass particles that have sintered during firing after the sedimentation over the metallic substrate. Firing time has an important influence on the coating porosity because of the longer extension of the interfacial reaction between the Ti (substrate) and the $SiO_2$ (glass) to form the intermetallic compound, $Ti_5Si_3$. Firing time and different $SiO_2$ content do not significantly influence the amount of crystalline phase (2.4CaO 0.6$Na_2O$ $P_2O_5$) in the coating.

The coatings were sensitive to Vickers indentation subcritical crack growth in ambient air, showing typical behaviour described by the classic power-law crack velocity function. The lower $SiO_2$ content coating presented longer

cracks for any time after the indentation. This is consistent with the tensile residual stresses of this coating due to the larger thermal expansion mismatch with the Ti6Al4V substrate.

Both coatings were also sensitive to stress–corrosion ring cracking by Hertzian indentation in air, being more sensitive the one with lower $SiO_2$ content. This behaviour was also consistent with the subcritical crack growth and residual stresses results and was satisfactorily rationalized by fracture mechanics, considering that the ring crack is the result of the environmental assisted crack growth of a surface flaw under the radial tensile stress at the surface due to Hertzian contact loading and the residual stresses.

The $SiO_2$ content of the glass coatings used for biomedical applications is determinant for its final performance because, not only determines the bioactivity of the coated implant, but it also has a clear influence in the residual stresses due to the thermal expansion mismatch with the Ti6Al4V alloy. These residual stresses, together with the dependence of the corrosion sensitivity on the $SiO_2$ content, determine the stress–corrosion cracking response of these coatings.

## Acknowledgments

This work is supported by the Spanish Ministry of Science and Technology through Grant No. MAT202-00368, the Generalitat de Catalunya through the Gaspar de Portolà exchange program, and the National Institutes of Health/National Institutes of Dental and Craniofacial Research through Grant No. IR01DE11289. J. Pavón wishes to thank Colciencias-Colombia for financial sponsorship of his Ph.D. studies.

## References

1. The ASM Committee on Titanium and Titanium Alloys, Properties of titanium and titanium alloys. In Metals Handbook, Vol. 3. Properties and Selection: Stainless Steels, Tool Materials and Special-Purpose Metals. American Society for Metals, Metals Park, Ohio, 1980, pp. 372–412.
2. Dobbs, H. S., Fracture of titanium orthopaedic implants. *J. Mater. Sci.*, 1982, **17**, 2340–2398.
3. Hench, L. L., Bioceramics: from concept to clinic. *J. Am. Ceram. Soc.*, 1991, **74**, 1487–1510.
4. Suchanek, W. and Yoshimura, M., Processing and properties of hydroxiapatite-based biomaterials for use as hard tissue replacement implants. *J. Mater. Res.*, 1998, **13**, 94–117.
5. Lacefield, W. R., Hydroxilapatite coating. In *An Introduction to Bioceramics*, ed. L. L. Hench and J. Wilson. World Scientific, Singapore, 1993, pp. 223–238.
6. Hastings, G. W., Dayli, D., and Mores, S., In *Bioceramics*. Vol. 1, ed. Ohnishi, H., Aoki, H. and Sawai, K. Euroamerica, Ishyaku, 1989, pp. 355–358.
7. Cook, S. D., Thomas, K. A., Dalton, J. E., Volkman, T. K., Whitecloud, T. S. and Kay, J. F., *J. Biomed. Mater. Res.*, 1993, **27**, 1501–1507.
8. Hench, L. L. and Anderson, O., Bioactive glass coatings. In *An Introduction to Bioceramics*, ed. L. L. Hench and J. Wilson. World Scientific, Singapore, 1993, pp. 239–260.
9. Lee, T. M., Chang, E., Wang, B. C. and Yang, C. Y., Characteristics of plasma-sprayed bioactive glass coatings on Ti6Al4V alloy: an in vitro study. *Surf. Coat. Technol.*, 1996, **79**, 170–177.
10. Kitsugi, T., Nakamura, T., Oka, M., Senaha, Y., Goto, T. and Shibuya, T., Bone-bonding behaviour of plasma-sprayed coatings of Bioglass®, AW-glass ceramic and tricalcium phosphate on titanium alloy. *J. Biomed. Mater. Res.*, 1996, **30**, 261–269.
11. Gómez-Vega, J. M., Saiz, E. and Tomsia, A. P., Glass-based coatings for titanium implant alloys. *J. Biomed. Mater. Res.*, 1999, **46**, 549–559.
12. Pazo, A., Saiz, E. and Tomsia, A. P., Silicate glass coatings on Ti-based implants. *Acta Mater.*, 1998, **46**, 2551–2558.
13. Pazo, A., Saiz, E. and Tomsia, A. P., Bioactive coatings on Ti and Ti6Al4V alloys for medical applications. In *Ceramic Microstructures: Control at Atomic Level*, ed. A. P. Tomsia and A. M. Glaeser. Plenum Press, Berkeley, 1998, pp. 543–550.
14. Hench, L. L., Splinter, R. J., Allen, W. C. and Greenlee, T. K., *J. Biomed. Res. Symp.*, 1971, **2**(1), 117.
15. Lawn, B. R., Ceramic-based layer structures for biomechanical applications. *Curr. Opin.: Solid State Mater. Sci.*, 2002, **6**, 229–235.
16. Klug, G. and Alexander, M., Kinematics theory on quantitative analysis of X-ray diffraction. In *Quantitative X-ray Diffractometry*, ed. L. S. Zevin and G. Kimmel. Springer-Verlag, NY, 1995, pp. 147–182.
17. Cullity, B. D., *Elements of X-ray Diffraction* (*2nd ed.*). Adison-Wesley, NY, 1978, pp. 315–378.
18. Noyan, I. C. and Cohen, J. B., *Residual Stress. Measurement by Diffraction and Interpretation*. Springer-Verlag, NY, 1987, pp. 117–140.
19. Whiters, P. J. and Badhesia, H. K., Overview: residual stress. Part 1—measurement techniques. *Mater. Sci. Tech.*, 2001, **17**, 355–365.
20. Malzbender, J., den Tooder, J. M. J., Blakenende, A. R. and de With, G., Measuring mechanical properties of coatings: a methodology applied to nano-particle-filled sol-gel coatings on glass. *Mater. Sci. Eng. R.*, 2002, **36**, 47–103.
21. Turner, P. S., *J. Res. NBS*, 1946, **37**, 239.
22. Lopez-Esteban, S., Saiz, E., Fujino, S., Oku, T., Suganuma, K. and Tomsia, A. P., Bioactive glass coatings for orthopedic metallic implants. *J. Eur. Ceram. Soc.*, 2003, **23**, 2921–2930.
23. Jackson, M. J. and Mills, B., Thermal expansion of alumino-alkasilicate and alumino-borosilicate glasses—comparison of empirical model. *J. Mater. Sci. Lett.*, 1997, **16**, 1264–1266.
24. Hall, F. P., The influence of chemical composition on the physical properties of glasses. *J. Am. Ceram. Soc.*, 1930, **13**, 182.
25. English, S. and Turner, W. E. S., Relationship between chemical composition and the thermal expansion of glasses. *J. Am. Ceram. Soc.*, 1927, **10**, 122.
26. Winkelmann, A. and Schott, O., Expansion coefficients of glasses. *Ann. Physik.*, 1894, **51**, 730.
27. Rhee, Y. W., Kim, H., Den, Y. and Lawn, B. R., Contact induced damage in ceramic coatings on compliant substrate: fracture mechanics and design. *J. Am. Ceram. Soc.*, 2001, **84**(5), 1066–1072.
28. Lawn, B. R., *Fracture of Brittle Solids* (*2nd ed.*). Cambridge University Press, Cambridge, 1993, pp. 249–299.
29. Warren, P. D., Determining the fracture toughness of brittle materials by Hertzian indentation. *J. Eur. Ceram. Soc.*, 1995, **15**, 201–207.
30. Roberts, S. G., Lawrence, C. W., Bisrat, Y., Warren, P. D. and Hills, D. A., Determination of surface stresses in brittle materials by Hertzian indentation: theory and experiment. *J. Am. Ceram. Soc.*, 1999, **82**(7), 1809–1816.

31. Licht, V., Hülsmeier, P. and Fett, T., Probability of cone crack initiation due to the spherical contact loading. *J. Eur. Ceram. Soc.*, 2004, **24**, 2907–2915.
32. Huber, M. T., Zur Theorie der Berührung Fester Elasticher Körper. *Ann. Phys. (Leipzig)*, 1940, **43**(61), 153–163.
33. Fett, T. and Munz, D., Local stress intensity factors for small semi-elliptical cracks under exponentially distributed stresses. *Eng. Fract. Mech.*, 1999, **64**, 105–116.
34. Timoshenko, S. and Goodier, J. N., *Theory of Elasticity* (*2nd ed.*). McGraw-Hill, N.Y, 1951, pp. 255–289.
35. Frank, F. C. and Lawn, B. R., On the theory of Hertzian fracture. *Proc. R. Soc. Lond.*, 1967, **A299**, 291–306.
36. Barry, C. and Nicholson, P. S., Stress–corrosion cracking of a bioactive glass. *Adv. Ceram. Mater.*, 1998, **3**(2), 127–130.